# Study of the photocatalysis and increase of antimicrobial properties of $Fe^{3+}$ and $Pb^{2+}$ co-doped ZnO nanoparticles obtained by microwave-assisted hydrothermal method

N.F. Andrade Neto[a,*], K.N. Matsui[b], C.A. Paskocimas[a], M.R.D. Bomio[a], F.V. Motta[a]

[a] LSQM, DEMAT, UFRN, Av. Sen. Salgado Filho, 3000, CEP 59072-970 Natal, RN, Brazil
[b] LabCQ, DEQ, UFRN, Av. Sen. Salgado Filho, 3000, CEP 59072-970 Natal, RN, Brazil

## ARTICLE INFO

## ABSTRACT

The difficulty in treating organic effluents and increasing the resistance of microorganisms to conventional treatments promotes the development of new materials for these applications. In this work, it was obtained ZnO co-doped with $Fe^{3+}$ and $Pb^{2+}$ (ZnO:xFe:yPb, with x and y varying between 0, 1, 3 and 7 mol%) by microwave-assisted hydrothermal method with a reaction temperature of 140 °C for 30 min. The powders were characterized by X-ray diffraction (XRD), field-scanning electron microscopy (SEM), Brunauer-Emmett-Teller method (BET), ultraviolet diffuse reflectance spectroscopy (DRS-UV), X-ray fluorescence analysis (XRF) and Fourier transform infrared spectroscopy (FTIR). Photocatalytic properties were estimated by the degradation of the methylene blue dye when subjected to UV radiation. The antimicrobial properties were investigated by the formation of inhibition halos against *E. coli* and *S. aureus* bacteria. The XRD patterns show that there was no formation of secondary phases, obtaining only the ZnO phase, with hexagonal structure. Through the XRD, it can be seen that the intensity of the characteristic peaks is also reduced as the dopant concentration increases, indicating the appearance of defects in the crystalline lattice. SEM images show that an increase in the dopant concentration promotes a loss in the morphology of ZnO nanoparticles, accompanied by a reduction in their mean size. The co-doping reduces the photocatalytic activity of ZnO against the methylene blue dye, but increases the antimicrobial activity against *E. coli* and *S. aureus* bacteria.

## 1. Introduction

According to reports from the World Health Organization (WHO), infectious diseases are the third largest cause of mortality in the world. Over the years, it has been reported an increase in the resistance of bacterial pathogens to the conventional antimicrobial agents [1,2]. Bacteria such as *Escherichia coli* and *Staphylococcus aureus* are among the pathogens that have most developed resistance to conventional remedies [3]. Besides the increase in health risks due to the increase in the resistance of pathogens to antibiotics, the expenses related to medical care related to drug inefficiency are also increased [4]. The best way to combat these increasingly strong pathogens is to develop new classes of antimicrobial agents. However, such development takes time and these new agents have limited time, since the pathogens will acquire resistance over time [5,6]. Therefore, there is a need in the development of low cost antimicrobial agents that do not allow bacterial evolution. Metals such as silver (Ag), copper (Cu), zinc (Zn) and

magnesium (Mg) are used to treat diseases before the revolution of pharmaceutical antibiotics [7]. Studies report that ZnO exhibits good antimicrobial activity and photochemical stability [8–10]. In addition, its antimicrobial efficiency can be attributed to its hydrophobicity and high oxidant power [11,12]. When ZnO is subjected to radiation with sufficient energy to overcome the band gap ($\sim 3.2$ eV), as UV radiation, it generates electron/hole pairs ($e^-/h^+$) by exciting the electron of the valence band to the conduction band, producing reactive oxygen species (ROS), such as hydroxyl ($^\cdot$OH) and superoxide ($O_2^{\cdot-}$) radicals, leading to microbial death [13–15]. Doping of ZnO with materials such as iron and lead causes defects in the crystalline lattice of the material, thus generating more reactive oxygen species, increasing the antimicrobial activity of the compound [16,17].

In parallel to the antimicrobial properties, the photocatalytic property of semiconductor materials has also been deeply studied due to the difficulty in the treatment of effluents, especially those from textile industries, because they have -N = N- groups linked to aromatic

rings, making conventional methods not effective [18]. The heterogeneous photocatalysis, which occurs in the presence of a semiconductor, usually in the solid state, is based on the same principle of action of the antimicrobial activity, having its efficiency directly linked to the generation of $e^-/h^+$ pairs and the impediment of their recombination [19,20]. The ZnO doping can be made with several materials aiming an increase for defects in the lattice and, consequently, greater generation of $e^-/h^+$ pairs and reduction in its band gap energy (Egap) [21,22]. Among these materials, the transition metals like Fe, Co, Ni, Cu, Cd, Ag, Bi, Pb, stand out [22–26].

Fe and Pb have the ability to generate defects in the ZnO lattice even in small concentrations, increasing its absorption range [27]. In addition, such transition metals exhibit high antimicrobial properties, destroying the cytoplasmic membrane of bacteria [28]. The codoping with Fe and Pb provides synergetic effect in the generation of defects, for degradation of recalcitrant pollutants and antimicrobial action [29]. In purpose to produce materials with high antimicrobial potential at a low cost, it was studied the antimicrobial activity and photocatalytic properties of $ZnO:xFe^{3+}:yPb^{2+}$ nanoparticles (with x and y ranging from 0, 1, 3 and 7 mol%) obtained by the microwave assisted hydrothermal method. The nanoparticles were characterized by X-ray diffraction (XRD), Fourier transform infrared spectroscopy (FTIR), ultraviolet diffuse reflectance spectroscopy (DRS-UV) and field emission scanning electron microscopy (SEM). The photocatalytic activity was estimated by the degradation of the methylene blue dye. The antimicrobial activity was estimated against *Escherichia coli* (gram negative) and *Staphylococcus aureus* (gram positive) bacteria.

## 2. Materials and methods

$Zn(NO_3)_2 \cdot 6H_2O$ (Sigma-Aldrich, 98%), $Fe(NO_3)_3 \cdot 9H_2O$ (Sigma-Aldrich, 98%), $Pb(NO_3)_2$ (Sigma-Aldrich, 99%), NaOH (Synth, 98%) and deionized water were used as precursor materials.

Co-doped zinc oxide powders were synthesized by the microwave assisted hydrothermal method. Pure ZnO was prepared for comparison, for this purpose, 0.0123 mol of $Zn(NO_3)_2 \cdot 6H_2O$ was dissolved in 70 mL of deionized water, the pH was set to 13 using NaOH. The mixture was transferred to a Teflon autoclave that was sealed and the system was heated under hydrothermal conditions using microwave radiation (2.45 GHz and maximum power of 800 W) at 140 °C for 30 min. The pressure inside the autoclave remained fixed at 3 atm. The product obtained was centrifuged and washed with deionized water and dried at 100 °C.

It was used $Pb(NO_3)_2$ and $Fe(NO_3)_3 \cdot 9H_2O$ for the preparation of the co-doped samples. First, the $Fe^{3+}$ ion concentration was fixed at 1 mol % and $Pb^{2+}$ was varied at 0, 1, 3 and 7 mol% ($ZnO:1\%Fe^{3+}:yPb^{2+}$ with y = 0, 1, 3 and 7 mol%). Subsequently, the $Pb^{2+}$ concentration was set at 1 mol% and $Fe^{3+}$ was varied at 0, 1, 3 and 7 mol% ($ZnO:1\% Pb^{2+}:xFe^{3+}$ with x = 0, 1, 3 and 7 mol%). $Zn(NO_3)_2 \cdot 6H_2O$ was dissolved into 50 mL of deionized water, obtaining solution 1. At the same, $Fe(NO_3)_3 \cdot 9H_2O$ and $Pb(NO_3)_2$ were dissolved into 20 mL of deionized water, obtaining solution 2. Then, solution 2 was poured into solution 1 and kept under stirring. NaOH was used to set its pH to 13. The mixture followed the same procedure as the ZnO synthesis. Thus, it was obtained the samples: ZnO:1%Fe (Z1F), ZnO:1%Fe:1%Pb (Z1F1P), ZnO:1%Fe:3%Pb (Z1F3P), ZnO:1%Fe:7%Pb (Z1F7P), ZnO:1%Pb (Z1P), ZnO:1%Pb:3%Fe (Z1P3F) and ZnO:1%Pb:7%Fe (Z1P7F).

The phases obtained for the $ZnO:xFe^{3+}:yPb^{2+}$ powders (with x and y varying between 0, 1, 3 and 7 mol%) were investigated using the Shimadzu diffractometer (XRD-6000) using CuKα radiation (1.5418 Å) with 2theta varying from 20° to 80°, step of 0.02° and a speed of 1°/min. For a better verification of the changes promoted by doping, the Rietveld refinement was performed using the General Structure Analysis System (GSAS) program with graphic interface EXPGUI [30]. SEM was performed in the Supra 35 (Zeiss) microscope to observe the morphology of the particles. Specific surface areas of the powders were

calculated by BET (Brunauer-Emmett-Teller) method from the adsorption isotherms in Belsorp II equipment (Bel Japan, INC). FTIR technique was performed using the Shimadzu IRTracer-100 equipment, with scanning from 500 to 4000 cm$^{-1}$. UV–vis spectroscopy was performed on the Shimadzu equipment (UV-2550), with a wavelength range between 200 and 900 nm and programmed for the diffuse reflectance mode, reflectance data were converted to absorbance by the Kubelka-Munk function [31] and the Wood and Tauc [32] equation was used to estimate Egap. Elemental X-ray fluorescence analysis (XRF) was performed on the Shimadzu EDX-720 spectrometer to analyze the chemical stability of the compounds.

The photocatalytic properties of the pure and doped ZnO powders, as a catalyst, were estimated by the degradation of the methylene blue (MB) dye of molecular formula $[C_{16}H_{18}ClN_3S]$ (99.5% purity, Mallinckrodt), at pH 5 with maximum absorption in 650 nm, illuminated by UV lamps, in aqueous solution. It was put 50 mL of the MB solution ($1 \times 10^{-5}$ mol/L concentration) and 0.05 g of the material to be tested in a quartz beaker. This mixture was kept under controlled temperature (25 °C) and illuminated by six UVC lamps (15 W TUV Philips, with maximum intensity of 254 nm = 4.9 eV). The sample was kept under stirring for 15 min, with the lights off, to disregard possible adsorption events. With the lamps on, samples were taken at 15 min intervals to monitor the variation of the absorption band of MB in the Shimadzu spectrophotometer (model UV-2600). The percentage of mineralization was estimated by the total amount of organic carbon obtained through the TOC analyzer Shimadzu 500. Mineralization degrees (%) were evaluated by the TOC values upon 90 min of illumination.

The antimicrobial properties of the powders were evaluated by in vitro tests, using agar diffusion method, against *E. coli* (ATCC-25922) and *S. aureus* (ATCC-25923) bacteria, following standard procedures stipulated by the Institute of Clinical and Laboratory Standards (CLSI), similar to the study by Araújo et al. [33]. The inoculum was prepared by direct suspension of the colonies in phosphate-buffered saline (PBS) on a water plate for 24 h at 35 °C. The turbidity of the solution was then adjusted according to the McFarland scale (bacterial density of $1.10^8$ CFU/mL). The test was performed using the well diffusion technique with 6 mm wells and adding 50 μL aliquots of the samples. For standard, antibiotics Gentamicin (10 mg/mL) and Vancomycin (30 mg/mL) were used for *E. coli* and *S. aureus*, respectively.

## 3. Results and discussions

The X-ray diffraction technique was used for crystallographic characterization and composition of $ZnO:xFe^{3+}:yPb^{2+}$ powders (with x and y ranging from 0, 1, 3 and 7 mol%). Fig. 1 shows the XRD patterns obtained for the samples synthesized in this study. In all samples, the presence of the diffraction peaks at 2θ = 31.79, 34.44, 36.28, 47.57, 56.65, 62.91, 66.44, 68.01, 69.15, 72.62 and 77.03°, refer to the characteristic planes (010), (002), (011), (012), (110), (013), (020), (112), (021), (004) and (022), respectively. The ZnO phases have a hexagonal system with space group *P*63*mc* (No. 186), characterized by ICSD 94004. Through the analysis of these patterns, it was concluded that co-doping occurred successfully, where there was no formation of secondary phases. Bazazi et al. [34] obtained ZnO without the presence of secondary phases via the hydrothermal method using NaOH and KOH to regulate the pH of the environment. Fig. 1 shows the reduction in the intensity of the ZnO characteristic peaks as the concentration of the doping cations increases, indicating an increase in the structural disorder. Guendouz et al. [35] observed that ZnO samples doped with 2% of $Al^{3+}$ and co-doped with 5% of $Sn^{4+}$ present a decrease in crystallinity due to the tensions caused in the crystalline lattice caused by the different ionic rays.

The Rietveld refinement was used to analyze possible differences in the structural arrangements induced by the addition of $Fe^{3+}$ and $Pb^{2+}$ in the ZnO lattice [36]. The ICSD 94004 was used for refinement. The
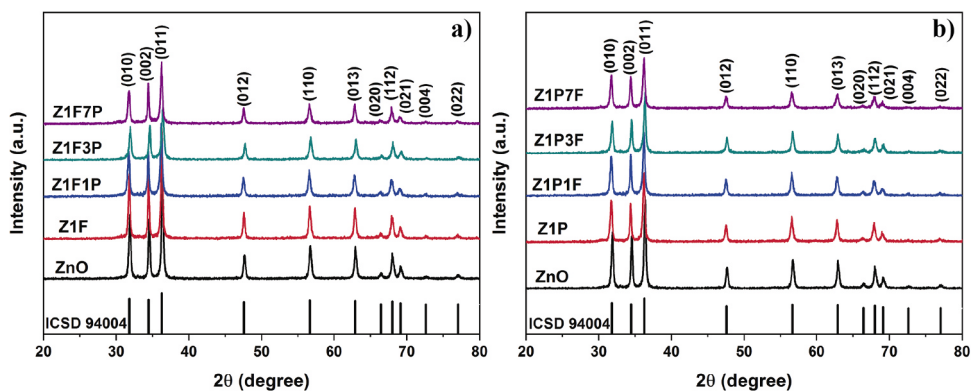
**Fig. 1.** XRD patterns obtained for samples of pure ZnO and co-doped with $Fe^{3+}$ and $Pb^{2+}$.
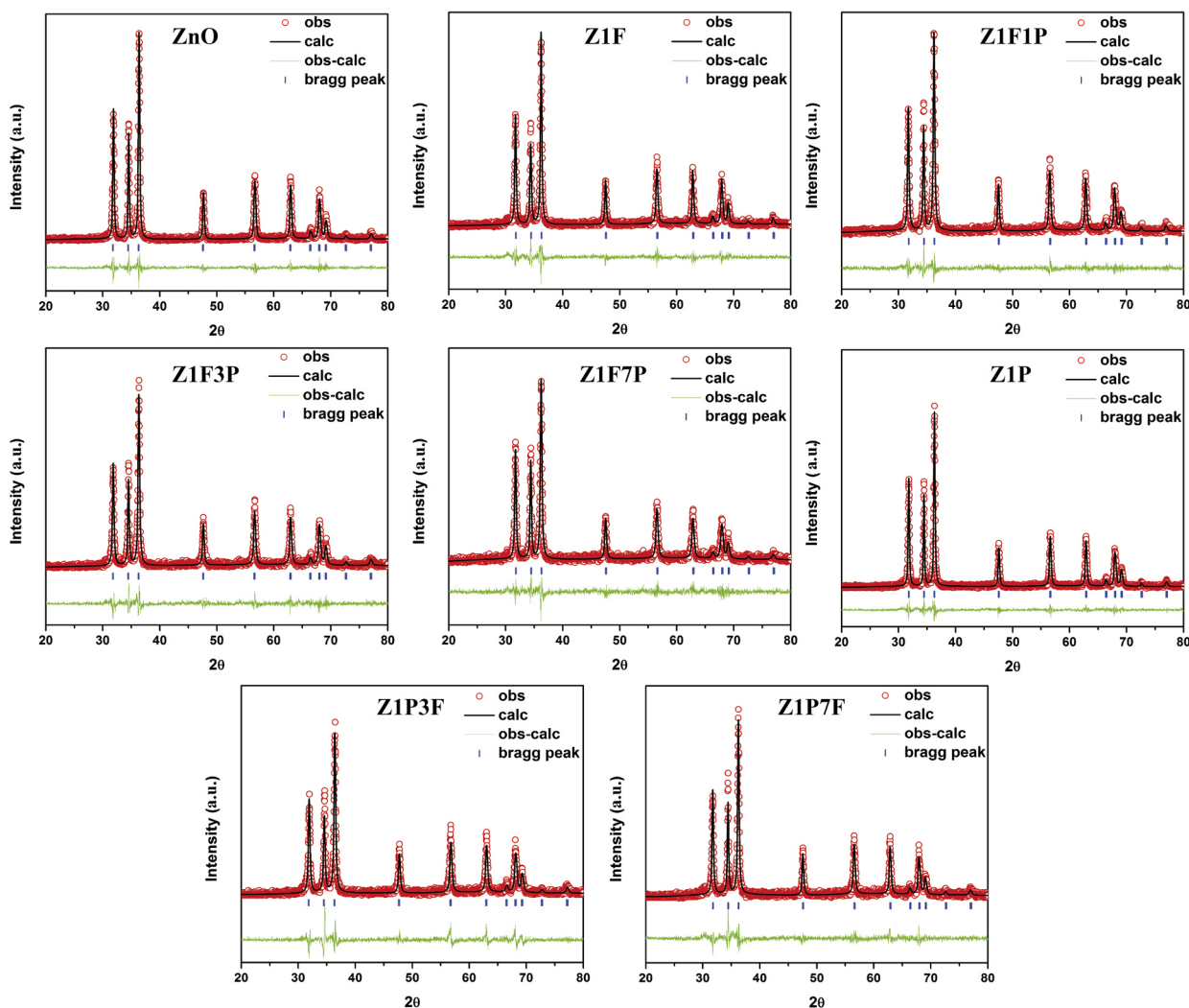


**Fig. 2.** Rietveld refinement for ZnO, Z1F, Z1F1P, Z1F3P, Z1F7P, Z1P, Z1P3F and Z1P7F samples.

parameters used for refining were: scale factor and phase fraction; background, which was modeled using a displaced Chebyshev polynomial function; peak shape, which was modeled using Thomson-Cox-Hasting pseudo-Voigt; change in lattice constants; fractional atomic coordinates; and isotropic thermal parameters. The results of the Rietveld refinement are shown in Fig. 2 and Table 1.

Due a small difference obtained between the curves observed (obs) and theoretically calculated (calc), it is concluded that the diffraction patterns of the samples are well adapted to the ICSD 94004. The quality

of the refinement was measured through the reliability parameters $\chi^2$, Rwp and Rp, which relate the differences between the observed (obs) and calculated (calc) curves. Reliability parameters with low values indicate good structural refinement quality. These data confirm that the samples are isostructural, being the crystals well adapted to the hexagonal structure with the *P63mc* spatial group (No. 186). The values obtained from the occupation of the $Zn^{2+}$, $Fe^{3+}$ and $Pb^{2+}$ cations in the unit cell are close to the synthesis stoichiometric, confirming that doping was successful.

**Table 1**
Rietveld refined structural parameters for the $ZnO:xFe^{3+}:yPb^{2+}$.

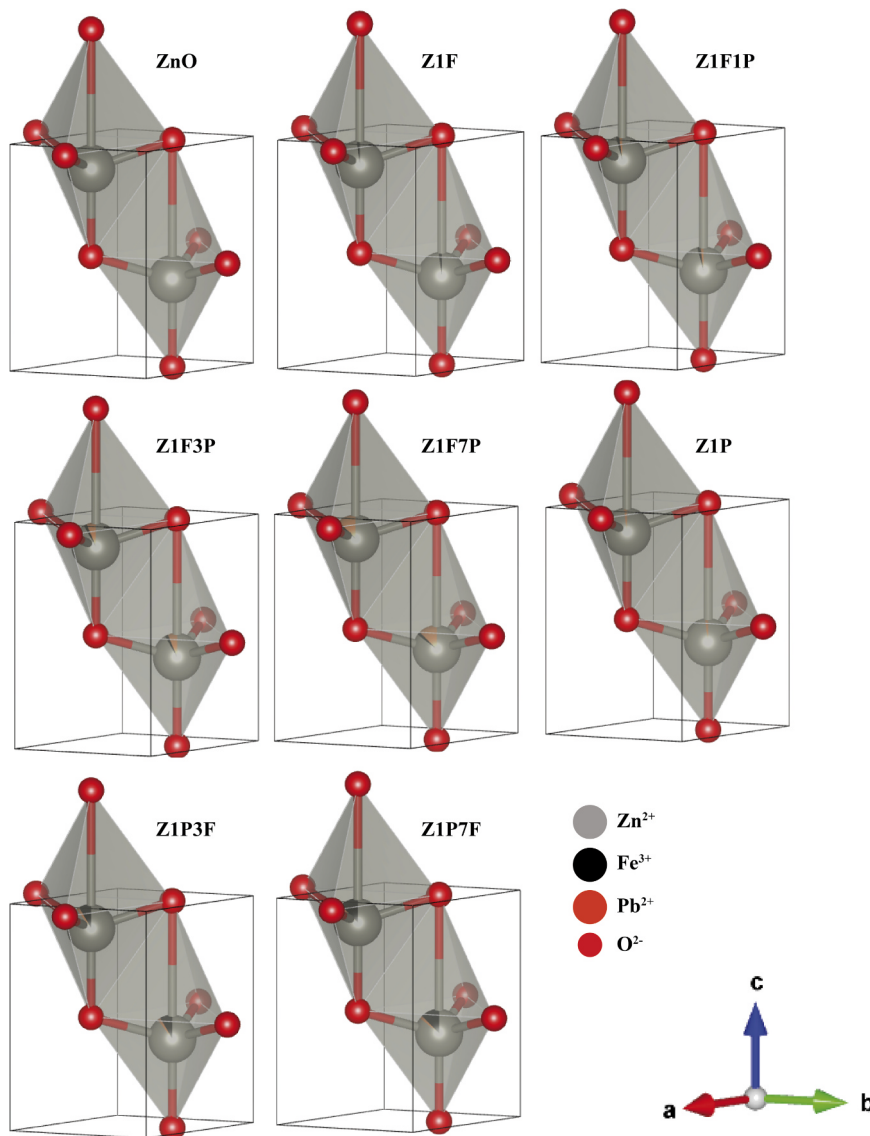| Sample | | ZnO | Z1F | Z1F1P | Z1F3P | Z1F7P | Z1P | Z1P3F | Z1P7F |
|---|---|---|---|---|---|---|---|---|---|
| $a$ (Å) | | 3.2515 | 3.2519 | 3.2522 | 3.2527 | 3.2525 | 3.2522 | 3.252 | 3.2465 |
| $c$ (Å) | | 5.2081 | 5.2065 | 5.2072 | 5.2075 | 5.209 | 5.2089 | 5.2067 | 5.203 |
| Cell Volume (Å$^3$) | | 55.0614 | 55.058 | 55.0755 | 55.0956 | 55.1047 | 55.0935 | 55.0365 | 54.8384 |
| Crystallite size (nm) | | 31.08 | 28.55 | 24.64 | 24.42 | 22.07 | 26.38 | 23.79 | 19.75 |
| Microstrain ($\times 10^3$) | | 0.2534 | 0.8033 | 0.2375 | 0.2187 | 1.2536 | 0.1049 | 0.1931 | 0.2455 |
| $\chi^2$ | | 1.347 | 1.450 | 1.231 | 1.335 | 1.269 | 1.350 | 1.507 | 1.391 |
| $R_{wp}$ | | 0.2149 | 0.2272 | 0.2053 | 0.2350 | 0.2189 | 0.2103 | 0.2414 | 0.2416 |
| $R_p$ | | 0.1440 | 0.1646 | 0.1473 | 0.1674 | 0.1582 | 0.1438 | 0.1737 | 0.1736 |
| Occ | $Zn^{2+}$ | 1 | 0.0845 | 0.9712 | 0.9611 | 0.9206 | 0.9879 | 0.9565 | 0.9086 |
| | $Fe^{+3}$ | 0 | 0.0155 | 0.0144 | 0.0097 | 0.0099 | 0 | 0.0294 | 0.0763 |
| | $Pb^{2+}$ | 0 | 0 | 0.0144 | 0.0292 | 0.0695 | 0.0121 | 0.0141 | 0.0152 |



**Fig. 3.** Model of hexagonal structure for ZnO, Z1F, Z1F1P, Z1F3P, Z1F7P, Z1P, Z1P3F and Z1P7F samples.

Table 1 shows the volume variation of the unit cell of the samples. It is possible to observe a reduction in their volume with the addition of the $Fe^{3+}$ dopant and an increase in the volume as the amount of $Pb^{2+}$ increases. This fact occurs due to the substitution of $Zn^{2+}$ cations by $Fe^{3+}$ and $Pb^{2+}$, which have ionic radii of 0.74, 0.645 and 1.19 Å, respectively. The increase for dopant promotes an increase in the number of defects in the crystalline lattice of the ZnO, thus generating smaller

crystallite sizes. Such behavior is in agreement with Vegard's law, in which, for solid metal solutions, the dimensions of the unit cell tend to decrease as the dopant concentration increases [37,38].

There were no changes in the x, y and z positions occupied by the $Zn^{2+}/Fe^{3+}/Pb^{2+}$ cations in the unit cell, being x = 0.3333, y = 0.6667 and z = 0.3812. The anions $O^{2-}$ maintained their positions in the x and y axes, being 0.3333 and 0.6667, respectively. The position in the z axis
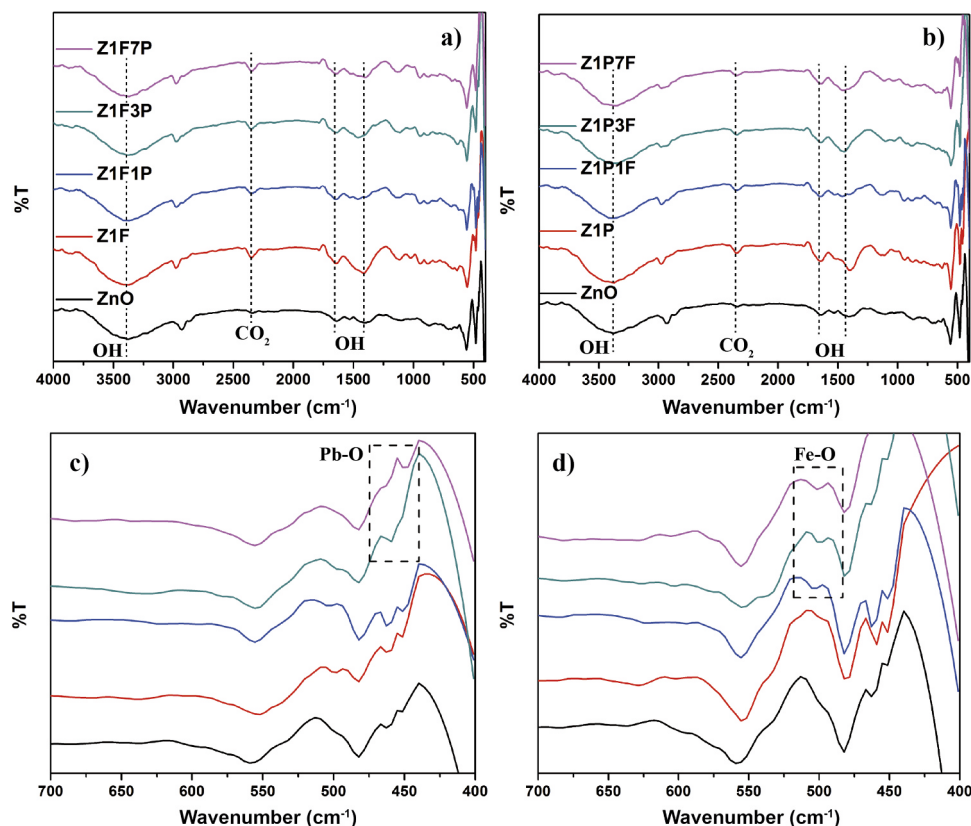
**Fig. 4.** FTIR spectra obtained for ZnO, Z1F, Z1F1P, Z1F3P, Z1F7P, Z1P, Z1P3F and Z1P7F samples.

varied, where the positions were -0.004493, -0.004725, -0.001014, -0.010936, -0.014434, -0.004623, -0.008282 and -0.008912 for the samples ZnO, Z1F1P, Z1F3P, Z1F7P, Z1P, Z1P3F and Z1P7F, respectively. It can be seen that the increase in the dopant concentration causes a displacement in the direction of the z-axis, being this growth more accentuated for the cations of $Pb^{2+}$. In the compact hexagonal structure each atom of a given layer is directly below or above the interstices formed between the adjacent layers, where each atom tangents three atoms of the layer above, six atoms in their own plane and three atoms in the layer below their plane. Fig. 3 shows the unit cells of the samples, obtained from the Rietveld refinement data.

The Fourier Transform Infrared (FTIR) technique was used to determine the functional groups on the surface of the material. The FTIR spectrum was studied in the region of 4000–400 $cm^{-1}$. Fig. 4 shows the FTIR spectra obtained for the samples of pure ZnO and doped with $Fe^{3+}$ and $Pb^{2+}$. It is a general perception that bands appearing below 1000 $cm^{-1}$ are associated with the bonds among inorganic elements. Fig. 4 shows bands at 450, 460, 486 and 563 $cm^{-1}$ in all samples, such bands refer to the main stretching bands of Zn-O [39–42]. Fig. 4c shows the band intensity reduction at 450 and 460 $cm^{-1}$ for samples Z1F3P and Z1F7P, respectively, indicating the introduction of $Pb^{2+}$ cations into the ZnO lattice [21]. Fig. 4d shows the presence of a weak band at 500 $cm^{-1}$, such a band is associated with the elongation of Fe-O bond [43]. The addition of $Fe^{3+}$ and $Pb^{2+}$ in the ZnO lattice promotes the appearance of a weak band at 1100 $cm^{-1}$ [44]. The bands present in all samples at 1440 and 1640 $cm^{-1}$ are due to the mode of vibration of the OH group relative to $H_2O$ adsorbed on the surface of ZnO [45]. As the bandwidth around 3300 $cm^{-1}$ is associated with the vibration of free water molecules and OH groups adsorbed on the surface of the oxide [46,47]. The absorption bands around 2343 $cm^{-1}$, present in all samples, are associated with the O-C-O molecules present in the atmosphere [39,40].

Field emission scanning electron microscopy (SEM) was used to observe possible changes in the ZnO morphology promoted by the addition of the $Fe^{3+}$ and $Pb^{2+}$ atoms. Fig. 5 shows the micrographs obtained by SEM for all study samples. The size of the ZnO nanoparticles was determined by the mean of their two largest dimensions, Fig. 6 shows the graphs the histograms of the nanoparticles size distribution of ZnO, Z1P7F and Z1F7P, respectively. Fig. 5a indicates that the microwave-assisted hydrothermal method favors the formation of nanoparticles of ZnO with nanoplates morphology with varying sizes. Despite the great variation in the dimensions of the nanoplates, the thickness remains with approximately 20 nm. Through the micrographs visual analysis, it can be seen that the increase of the dopant materials generates a loss of conformity in the morphology of the nanoparticles, accompanied by a reduction of their size, as shown in Fig. 6. The loss of morphological compliance and particle size reduction are more evident in samples Z1P3F and Z1P7F, as shown in Fig. 5e and g, respectively. Kumar et al. [23] observed that the addition of Fe atoms promotes a change in the morphology of ZnO nanoparticles, leaving their surface with a rough appearance. Feng et al. [48] showed that the doping with Fe generates a reduction of approximately $10\times$ in the size of the particles of $WO_3$ and a loss of their rectangular morphology for irregular morphologies. The minor alteration with the increase of the Pb amount is due to the fact of having the same valence, however, different ionic rays, which generate deformations in the lattice. Moreover, the increase of the $Pb^{2+}$ concentration generates a reduction of the free surface energy of the planes (100) and (002) and favors the growth of the planes (022) and (101), resulting in the morphological alteration of the nanoparticles [49]. The concentration of dopants is related to morphological changes, due to the appearance of defects in the crystalline lattice of the base compound, however, doping will not always result in a morphological alteration. Veerathangam et al. [50] reported that the addition of 2% Pb does not promote changes in the morphology of CdS thin films.

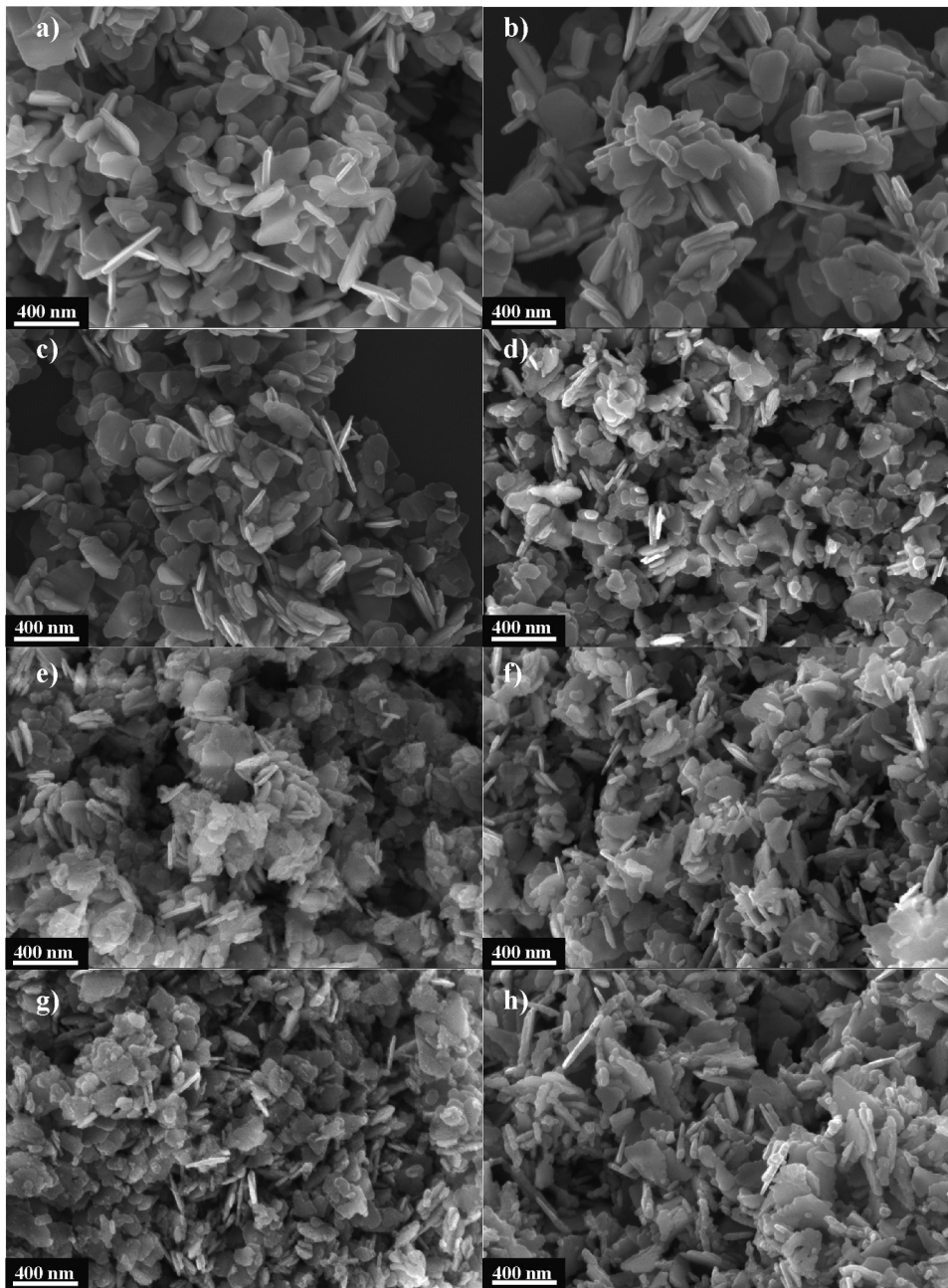X-ray spectroscopy was performed by energy dispersion (EDX) to

**Fig. 5.** Micrographies obtained by SEM for (a) ZnO, (b) Z1P, (c) Z1F, (d) Z1P1F, (e) Z1P3F, (f) Z1F3P, (g) Z1P7F and (h) Z1F7P samples.

confirm the presence of the dopants and mapping was performed to analyze the distribution of the atoms in the particles. Fig. 7a and b shows the areas used for EDX analysis and mapping (c and d), Fig. 7e and f shows the EDX spectra for ZnO and Z1P1F samples, respectively. The EDX spectra show the zinc and oxygen peaks for the ZnO sample, and the zinc, oxygen, iron and lead peaks for the Z1P1F sample. The silicon peak was disregarded for the analysis. The mappings show that the compounds appear uniformly distributed throughout all the particles.

The diffuse reflectance spectroscopy technique in the visible ultra-violet region was used to estimate the band gap (Egap) of pure and doped ZnO powders. The Kubelka-Munk function (Eq. (1)) [31] was used to convert the reflectance data to the absorbance data. The method of Wood and Tauc (Eq. (2)) [32] was used to estimate the value of the optical gap band (Egap).

$$F(R) = \frac{(1 - R)^2}{2R} = \frac{K}{S} \tag{1}$$

where: F(R) is the absorbance, R is the absolute reflectance, K is the absorption coefficient, and S is the scattering coefficient.

$$F(R)h\nu \propto (h\nu - Egap)^k \tag{2}$$

where: h is the Planck constant, $\upsilon$ is the frequency, F(R) is the absorbance and k is indicated for the different transitions (k = 1/2, 2, 3/2 or 3 for permissible direct, permissible indirect, direct prohibited and indirect prohibited, respectively). For the powders of pure and doped ZnO, k = ½ was allowed, that is, direct allowed. The graphs of the [F(R)h$\upsilon$]$^2$ versus photon energy (h$\upsilon$) were plotted, extrapolating the curve linear portion to zero absorption to estimate the Egap. Fig. 8 shows the graphs obtained for the pure ZnO, indicating how to obtain the values of Egap.
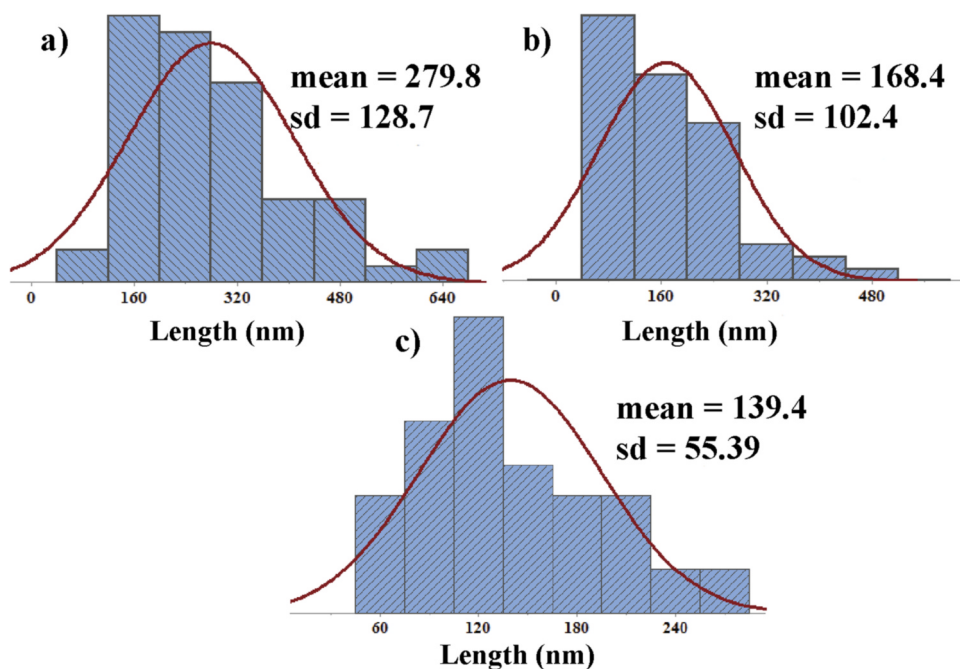
**Fig. 6.** Histogram of the nanoparticle length distributions for (a) ZnO, (b) Z1F7P and (c) Z1P7F samples.
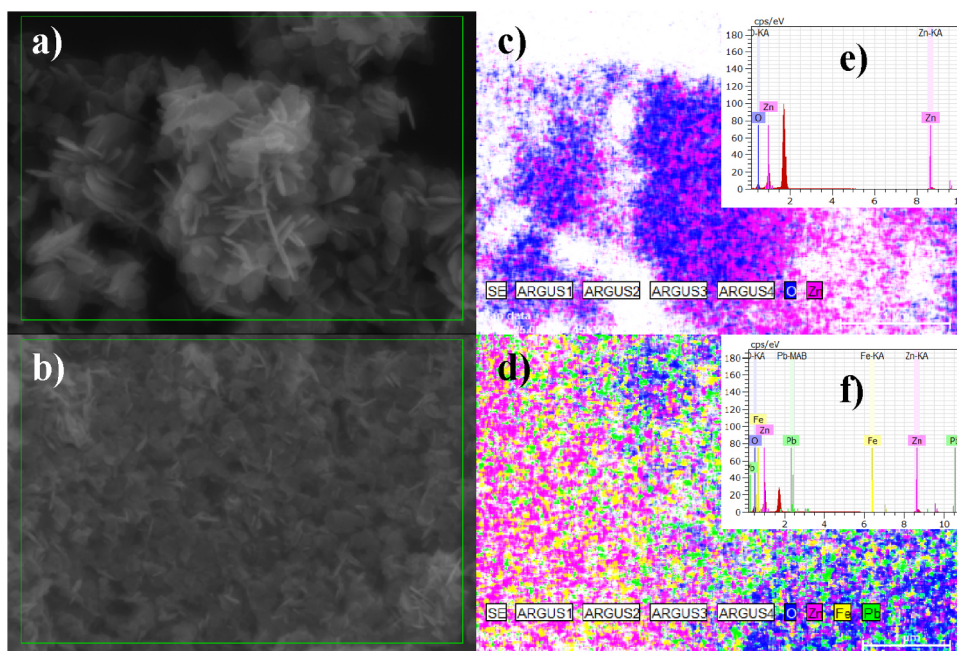


**Fig. 7.** Areas used for EDS analysis (a) and (b), mapping components (c) and (d) and EDS spectra (e) and (f) for ZnO and Z1P1F samples, respectively.

The direct Egap value found for ZnO was 3.15 eV, being in agreement with that reported in other studies. [51,52]. The gap energy of semiconductor materials is associated with the presence of defects in the crystalline lattice where they allow the formation of localized states in the forbidden band. The addition of electron-donor materials creates states near the conduction band, whereas electron-receiving materials create levels near the valence band [53]. Generally, the addition of large amounts of dopant occupy states near the conduction band and shift it to higher energies due to the Burstein-Moss effect. [54]. It was observed that the addition of $Fe^{3+}$ and $Pb^{2+}$ in the proportion of 8% reduces to Egap, indicating that there was creation of intermediate levels in the prohibited range without exceeding the concentration of charge carriers. The Z1P sample does not change the gap energy of ZnO.

The addition of $Fe^{3+}$ ions promotes the reduction of Egap in all samples, where it remained practically constant, around 3.06 eV. Normally, the reduction in crystallite size is expected to generate larger Egap, a fact opposite to that observed. Thus, the reduction in Egap is related to the electronic structure, with the decrease in the maximum valence band and the minimum conduction band, through the reduction of the conduction range Zn-s in relation to the vacuum level [55].

The photocatalytic activity of ZnO samples doped with $Fe^{3+}$ and $Pb^{2+}$ was estimated against the methylene blue dye (MB) discoloration under UV radiation, with a total test time of 90 min, being an aliquot of it withdrawn every 15 min Fig. 9a shows the variation of the absorbance of the MB when in contact with the Z1F sample under UV radiation. By the absorbance spectra obtained for all samples, the
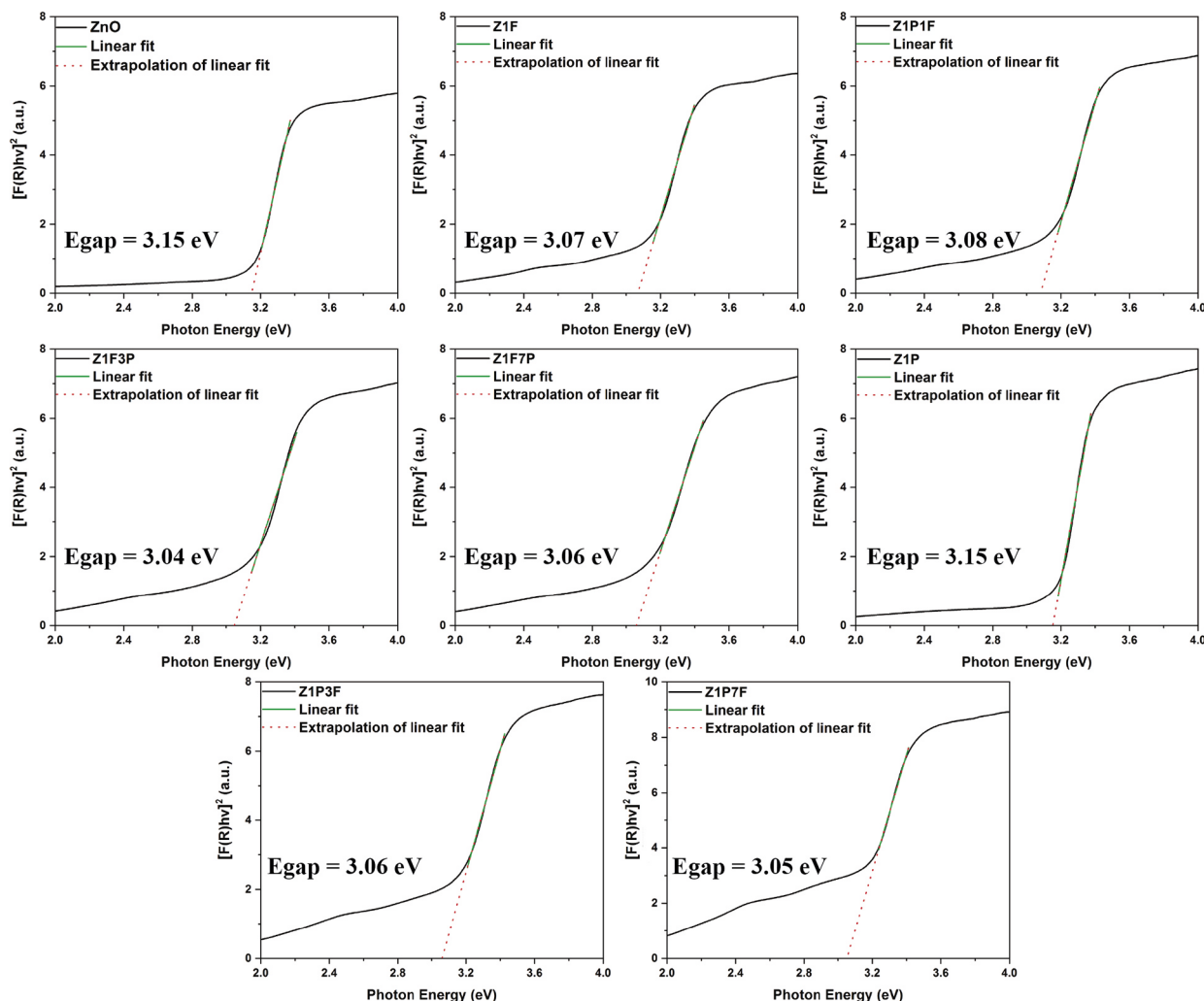
**Fig. 8.** Graphical representation of modified Kubelka-Munk function for determination of direct Egap of the ZnO samples.

concentration change curves were plotted by the test time. The variation of the dye concentration, with and without the presence of the catalyst, illuminated under UV radiation allows us to estimate the efficiency of its degradation. Fig. 9b and c show the variation of MB concentration by the test time. Fig. 9d shows the degraded percentage of the MB dye, in the period of 90 min, for all samples obtained in this work. The MB curves, shown in Fig. 9b and c, relate to photolysis of the methylene blue dye.

The reactions that describe the photocatalytic activity are shown in Eqs. (3)–(13). It is possible to observe that the $e^-/h^+$ pairs generated by the incidence of UV radiation provide the formation of ROS, which act to transform the dye into mineral acids, $CO_2$ and $H_2O$ (Eqs. (11)–(13)) [56].

$$Z1P1F + h\nu \rightarrow e^- \ (CB) + h^+ \ (VB) \tag{3}$$

$$O_2 + e^- \rightarrow O_2^{\bullet-} \tag{4}$$

$$Fe^{3+} + e^- \rightarrow Fe^{2+} \tag{5}$$

$$Fe^{2+} + O_2 \ (ads) \rightarrow Fe^{3+} + O_2^{\bullet-} \tag{6}$$

$$h^+ + H_2O \rightarrow H^+ + \ ^\bullet OH \tag{7}$$

$$O_2 + 2H^+ + 2e^- \rightarrow H_2O_2 \tag{8}$$

$$H_2O_2 + e^- \rightarrow \ ^\bullet OH + OH^- \tag{9}$$

$$h^+ + OH^- \rightarrow \ ^\bullet OH \tag{10}$$

$$MB + O_2^{\bullet-} \rightarrow CO_2 + H_2O + mineral \ acids \tag{11}$$

$$MB + h^+ \rightarrow CO_2 + H_2O + mineral \ acids \tag{12}$$

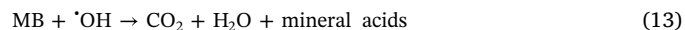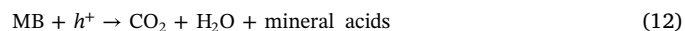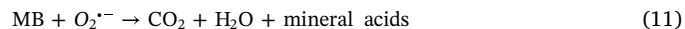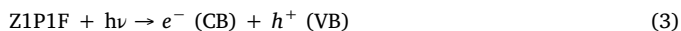$$MB + \ ^\bullet OH \rightarrow CO_2 + H_2O + mineral \ acids \tag{13}$$

Fig. 9 shows that the pure ZnO exhibits the best photocatalytic activity, completely degrading the MB after 90 min. The addition of $Fe^{3+}$ and $Pb^{2+}$ considerably reduces the photocatalytic capacity of ZnO. Z1P3F and Z1F7P samples presented the worst results, reducing the concentration of the MB solution in only 30.4% and 31.5%, respectively. Le et al. [57] showed that the addition of $Fe^{3+}$ atoms in the ZnO lattice suppresses its photocatalytic activity, making it a good material to be used in sunscreens. The photocatalytic activity of semiconductor materials is directly related to the impedance of the electron/hole pair ($e^-/h^+$) recombination, since they act in the generation of hydroxyl radicals ($^\bullet OH$) which are strong oxidizing agents of organic materials, such as dyes [58,59].

The addition of $Fe^{3+}$ atoms promotes the generation of defects in the ZnO lattice. These defects may act as the recombination center of the $e^-/h^+$ pairs, decreasing the photocatalytic activity of these compounds [57]. However, by varying the concentration of $Fe^{3+}$, it was observed that by increasing the concentration of 3% Fe (Z1P3F) to 7% (Z1P7F) there was an increase in the photocatalytic activity. Which may be related to the increase in the number of defects, where they stop acting as the recombination center of the $e^-/h^+$ pairs and act to prevent their recombination. In addition, the $Fe^{3+}$ ions can be reduced to $Fe^{2+}$ and reoxidized in $Fe^{3+}$ by the $O_2$ molecules in the environment, thus

**Fig. 9.** (a) Variation of the absorbance of MB for Z1F sample, (b) and (c) concentration variation by time when fixed the $Fe^{3+}$ and $Pb^{2+}$ ratios, respectively, and (d) percent degradation for all samples.



**Fig. 10.** Inhibition halos formed by all samples in this study against (a) E. coli and (b) S. aureus bacteria.

allowing the transmission of $e^-$. Therefore, a greater amount of $Fe^{3+}$ benefits the separation of the $e^-/h^+$ [60]. Eshaghi et al. [44] observed an increase in $Fe^{3+}$ concentration doping $TiO_2$ promotes a reduction in its photoluminescence intensity and an increase in its photocatalytic activity, indicating an increase in the rate of recombination of the $e^-/h^+$ pairs. The increase of the Pb concentration, from 1% to 3% and 7%, promotes an increase in the number of defects [21] and a reduction in the photocatalytic activity, indicating that these defects act as $e^-/h^+$ centers of recombination.

For more information on MB dye degradation, the final mineralization (after 90 min of photocatalytic test) was calculated from the TOC measurements for ZnO, Z1P3F, Z1F7P and MB (photolysis) samples. The methodology applied in this work was similar to the work

done by Liu et al. [61]. The results indicate that the ZnO sample, which presented the best results, mineralized approximately 95%, whereas the Z1P3F and Z1F7P samples mineralized about 39% and 40%, respectively, presenting the worst results for the tested powders. The curves traced only under UV radiation, referring to photolysis, mineralized only 2%. Fig. S1 shows the histograms obtained from the final TOC values.

Due to the high toxicity of Pb, it is essential that it is not released in the medium after the photocatalytic application. For more information about the chemical stability of the compounds, XRF analysis was performed before and after the photocatalytic test in the Z1F3P sample. According to Fig. S2, XRF analyzes before and after the photocatalytic test show the peaks related to Fe-kα, Fe-kβ, Zn-kα, Zn-kβ, Pb-Lα, Pb-

**Table 2**
Medium diameter (mm) and standard deviation of the inhibition halos obtained for samples of pure ZnO and doped with $Fe^{3+}$ and $Pb^{2+}$ regarding *E. coli* and *S. aureus* bacteria.

| Samples | Inhibition halos (mm) | |
|---|---|---|
| | *E. coli* | *S. aureus* |
| ZnO | 11.31 (0.42) | 12.03 (0.73) |
| Z1P | 11.51 (0.48) | 11.75 (0.94) |
| Z1F | 11.90 (0.70) | 11.93 (0.98) |
| Z1P1F | 12.13 (0.44) | 12.58 (0.99) |
| Z1P3F | 12.41 (0.58) | 14.24 (0.85) |
| Z1P7F | 12.78 (0.91) | 14.41 (0.89) |
| Z1F3P | 12.49 (0.72) | 13.76 (0.96) |
| Z1F7P | 12.62 (0.83) | 14.20 (0.93) |
| Gentamicin | 17.50 (0.98) | – |
| Vancomycin | - | 18.22 (0.81) |

Lβ1 and Pb-Lγ1 transitions. The percentages obtained are close to theoretical, indicating that good ion incorporation during doping. The small variation between the percentages before and after the photo-catalytic test indicates that there was no loss during the test, where the difference is associated to the equipment error.

Zeta potential of the ZnO, Z1P, Z1F, Z1P7F and Z1F7P samples in saline solution (pH 5) was estimated to obtain more information about the surface charger in the photocatalytic properties, obtaining values of -0.03, 3.67, 0.01, 3.91 and 6.62 mV, respectively. By means of the obtained values, it can be seen that the doping with $Fe^{3+}$ and $Pb^{2+}$ provides the increase of the zeta potential, indicating that the doped samples have isoelectric point above pH 5 [62]. MB dye has a cationic charge [63], so the positive potential on the surface of the nanoparticles of ZnO repulsively act the dye chains, damaging the photocatalytic activity.

The antimicrobial activity of the pure and doped ZnO samples doped with $Fe^{3+}$ and $Zn^{2+}$ was evaluated regarding *E. coli* (gram negative) and *S. aureus* (gram positive) by measuring the inhibition halo formed. For greater reliability of the inhibition halo values, all tests were performed in triplicate and the medium average was used. Vancomycin (*S. aureus*) and gentamicin (*E. coli*) antibiotics were used for comparison. The well diffusion technique was used and the diameters of the inhibition halos formed around the wells were measured. Fig. 10 shows the shape of the inhibition halos formed for the ZnO, Z1P7F and Z1F7P samples regarding *E. coli* (Fig. 9a) and *S. aureus* (Fig. 9b). Table 2 shows the mean diameters of inhibition halos for all samples in this study.

Through values of the diameters of inhibition halos shown in Table 2, it can be seen that the increase in the dopant concentration acts positively on the antimicrobial activity regarding *E. coli* and *S. aureus* bacteria. As previously seen, the addition of $Fe^{3+}$ and $Pb^{2+}$ generates a reduction in the size of the ZnO nanoparticles, promoting an increase in their surface area. According to the values presented in the adsorption curves (Fig. S3), Z1P7F sample present the largest surface area of 24.09 $m^2$ $g^{-1}$, followed by Z1F7P (14.04 $m^2$ $g^{-1}$) and ZnO (8.49 $m^2$ $g^{-1}$) samples. The surface area is an important variable in the antimicrobial activity of semiconductor materials, where its increase generates a greater area of direct contact with the bacteria, increasing its efficiency. Zare et al. [64] obtained ZnO nanoparticles of different sizes and concluded that the smaller nanoparticles had the best antimicrobial activities regarding *E. coli* and *S. aureus* bacteria.

In addition, performing doping and co-doping alters the generation and recombination of $e^-/h^+$ pairs, changing the properties dependent on this recombination. Nanoparticles of metal oxides meet bacteria to neutralize their high surface potential, generating $e^-/h^+$ pairs that act in the generation of ROS and the release of metal ions, which are highly toxic to bacteria [65]. The ZnO nanoparticles main mechanism of action is still unknown, however, the literature reports that direct or

electrostatic interaction between the nanoparticles and the cell surface, the production of reactive oxygen species (ROS) and the cellular internalization of ZnO nanoparticles are their main mechanisms [66–68]. ROS and metal ions act by deforming the cytoplasmic membrane of bacteria, leading to the leakage of intracellular substances and, consequently, the death of the bacteria [69,70]. Ma et al. [71] showed that increase of Fe concentration doping ZnO increases the ZnO antimicrobial efficiency against *C. albicans* and *A. flavus* bacteria, due to a higher generation of ROS.

## 4. Conclusion

The XRD patterns show that the hydrothermal method assisted by microwave is effective in obtaining ZnO nanoparticles co-doped with $Fe^{3+}$ and $Pb^{2+}$, without the formation of secondary phases. The increase in dopant concentration leads to a reduction in the intensity of diffraction peaks, indicating that there is a decrease in the organization in the ZnO crystalline lattice. The FTIR curves confirm the success of the doping, with the appearance of bands respective to the doping materials. The morphology of nanoplates was observed for ZnO samples, with a reduction in their average size as the dopant concentration increases, being this reduction more evident with the addition of $Fe^{3+}$, varying from 279.8 to 139.4 nm, for the ZnO and Z1P7F samples, respectively. The addition of $Fe^{3+}$ and $Pb^{2+}$ atoms leads to a reduction in the photocatalytic activity of the ZnO nanoparticles against the methylene blue dye. However, it increases the antimicrobial activity related to the *E. coli* and *S. aureus* bacteria.

## Appendix A. Supplementary materials

Supplementary data associated with this article can be found in the online version at doi:10.1016/j.mssp.2018.12.034.

## References

[1] M. Bilal, T. Rasheed, H.M.N. Iqbal, H. Hu, W. Wang, X. Zhang, Macromolecular agents with antimicrobial potentialities: a drive to combat antimicrobial resistance, Int. J. Biol. Macromol. 103 (2017) 554–574.

[2] M.H. Semreen, M.I. El-Gamal, S. Abdin, H. Alkhazraji, L. Kamal, S. Hammad, F. El-Awady, D. Waleed, L. Kourbaj, Recent updates of marine antimicrobial peptides, Saudi Pharm. J. 26 (2018) 396–409.

[3] G.H. Talbot, J. Bradley, J.J.E. Edwards, D. Gilbert, M. Scheld, J.G. Bartlett, Bad bugs need drugs: an update on the development pipeline from the antimicrobial availability task force of the infectious diseases society of America, Clin. Infect. Dis. 42 (2006) 657–668.

[4] A. Coates, Y. Hu, R. Bax, C. Page, The future challenges facing the development of new antimicrobial drugs, Nat. Rev. Drug Discov. 1 (2002) 895.

[5] C.L. Ventola, The antibiotic resistance crisis: Part 1: causes and threats, P&T 40 (2015) 277–283.

[6] D.I. Andersson, D. Hughes, Antibiotic resistance and its cost: is it possible to reverse resistance? Nat. Rev. Microbiol. 8 (2010) 260.

[7] K. Zheng, M.I. Setyawati, D.T. Leong, J. Xie, Antimicrobial silver nanomaterials, Coord. Chem. Rev. 357 (2018) 1–17.

[8] G.R. Navale, M. Thripuranthaka, D.J. Late, S.S. Shinde, Antimicrobial activity of ZnO nanoparticles against pathogenic bacteria and fungi, JSM Nanotechnol. Nanomed. 3 (2015).

[9] A. Zyoud, M. Dwikat, S. Al-Shakhshir, S. Ateeq, J. Shteiwi, A. Zu'bi, M.H.S. Helal, G. Campet, D. Park, H. Kwon, T.W. Kim, M. Kharoof, R. Shawahna, H.S. Hilal, Natural dye-sensitized ZnO nano-particles as photo-catalysts in complete degradation of E. coli bacteria and their organic content, J. Photochem. Photobiol. A: Chem. 328 (2016) 207–216.

[10] C. Lizama, J. Freer, J. Baeza, H.D. Mansilla, Optimized photodegradation of Reactive Blue 19 on TiO2 and ZnO suspensions, Catal. Today 76 (2002) 235–246.

[11] J. Zhang, G. Pu, S.J. Severtson, Fabrication of zinc oxide/polydimethylsiloxane composite surfaces Demonstrating oil-fouling-resistant superhydrophobicity, ACS Appl. Mater. Interfaces 2 (2010) 2880–2883.

[12] Y. Liu, Z. Lin, W. Lin, K.S. Moon, C.P. Wong, Reversible super-hydrophobic–superhydrophilic transition of ZnO nanorod/epoxy composite films, ACS Appl. Mater. Interfaces 4 (2012) 3959–3964.

[13] L. Zhang, Y. Jiang, Y. Ding, M. Povey, D. York, Investigation into the antibacterial behaviour of suspensions of ZnO nanoparticles (ZnO nanofluids), J. Nanopart. Res. 9 (2007) 479–489.

[14] L. Zhang, Y. Jiang, Y. Ding, N. Daskalakis, L. Jeuken, M. Povey, A.J. O'Neill, D.W. York, Mechanistic investigation into antibacterial behaviour of suspensions of ZnO nanoparticles against E. coli, J. Nanopart. Res. 12 (2010) 1625–1636.

[15] V.P. Singh, K. Sandeep, H.S. Kushwaha, S. Powar, R. Vaish, Photocatalytic, hydrophobic and antimicrobial characteristics of ZnO nano needle embedded cement composites, Constr. Build. Mater. 158 (2018) 285–294.

[16] A. Pugazhendhi, S.S. Kumar, M. Manikandan, M. Saravanan, Photocatalytic properties and antimicrobial efficacy of Fe doped CuO nanoparticles against the pathogenic bacteria and fungi, Microb. Pathog. 122 (2018) 84–89.

[17] D. Rehana, D. Mahendiran, R. Manigandan, V. Narayanan, A. Kalilur Rahiman, Evaluation of photocatalytic, antimicrobial and anticancer activities of ZnO/MS (M = Zn, Cd or Pb) core/shell nanoparticles, Mater. Sci. Eng.: B 225 (2017) 20–32.

[18] A. Kunz, P. Peralta-Zamora, S.Gd Moraes, N. Durán, Novas tendências no tratamento de efluentes têxteis, Quím. nova (2002).

[19] N.M. Mahmoodi, S. Keshavarzi, M. Ghezelbash, Synthesis of nanoparticle and modelling of its photocatalytic dye degradation ability from colored wastewater, J. Environ. Chem. Eng. 5 (2017) 3684–3689.

[20] X. Rong, F. Qiu, C. Zhang, L. Fu, Y. Wang, D. Yang, Preparation, characterization and photocatalytic application of TiO2–graphene photocatalyst under visible light irradiation, Ceram. Int. 41 (2015) 2502–2511.

[21] M. Sathya, K. Pushpanathan, Synthesis and optical properties of Pb doped ZnO nanoparticles, Appl. Surf. Sci. (2017).

[22] K. Vanheusden, W.L. Warren, J.A. Voigt, C.H. Seager, D.R. Tallant, Impact of Pb doping on the optical and electronic properties of ZnO powders, Appl. Phys. Lett. 67 (1995) 1280–1282.

[23] R. Kumar, A. Umar, D.S. Rana, P. Sharma, M.S. Chauhan, S. Chauhan, Fe-doped ZnO nanoellipsoids for enhanced photocatalytic and highly sensitive and selective picric acid sensor, Mater. Res. Bull. 102 (2018) 282–288.

[24] P. Pascariu, I.V. Tudose, M. Suchea, E. Koudoumas, N. Fifere, A. Airinei, Preparation and characterization of Ni, Co doped ZnO nanoparticles for photocatalytic applications, Appl. Surf. Sci. (2018).

[25] T.K. Pathak, H.C. Swart, R.E. Kroon, Influence of Bi doping on the structure and photoluminescence of ZnO phosphor synthesized by the combustion method, Spectrochim. Acta Part A: Mol. Biomol. Spectrosc. 190 (2018) 164–171.

[26] S.K. Kokate, A.T. Supekar, P.K. Baviskar, B.M. Palve, S.R. Jadkar, K.C. Mohite, H.M. Pathan, CdS sensitized pristine and Cd doped ZnO solar cells: effect of SILAR cycles on optical properties and efficiency, Mater. Sci. Semicond. Process. 80 (2018) 179–183.

[27] L. Liu, Z. Liu, Y. Yang, M. Geng, Y. Zou, M.B. Shahzad, Y. Dai, Y. Qi, Photocatalytic properties of Fe-doped ZnO electrospun nanofibers, Ceram. Int. 44 (2018) 19998–20005.

[28] L.B. Rice, Antimicrobial stewardship and antimicrobial resistance, Med. Clin. N. Am. 102 (2018) 805–818.

[29] X. Peng, Z. Wang, J. Huang, B.R. Pittendrigh, S. Liu, X. Jia, P.K. Wong, Efficient degradation of tetrabromobisphenol A by synergistic integration of Fe/Ni bimetallic catalysis and microbial acclimation, Water Res. 122 (2017) 471–480.

[30] B. Toby, EXPGUI, a graphical user interface for GSAS, J. Appl. Crystallogr. 34 (2001) 210–213.

[31] L. Tolvaj, K. Mitsui, D. Varga, Validity limits of Kubelka–Munk theory for DRIFT spectra of photodegraded solid wood, Wood Sci. Technol. 45 (2011) 135–146.

[32] D.L. Wood, J. Tauc, Weak absorption tails in amorphous semiconductors, Phys. Rev. B 5 (1972) 3144–3151.

[33] E. Araújo, A.S. Pimenta, F.M.C. Feijó, R.V.O. Castro, M. Fasciotti, T.V.C. Monteiro, K.M.G. Lima, Antibacterial and antifungal activities of pyroligneous acid from wood of Eucalyptus urograndis and Mimosa tenuiflora, J. Appl. Microbiol. 124 (2017) 85–96.

[34] S. Bazazi, N. Arsalani, A. Khataee, A.G. Tabrizi, Comparison of ball milling-hydrothermal and hydrothermal methods for synthesis of ZnO nanostructures and evaluation of their photocatalytic performance, J. Ind. Eng. Chem. 62 (2018) 265–272.

[35] H. Guendouz, A. Bouaine, N. Brihi, Biphase effect on structural, optical, and electrical properties of Al-Sn codoped ZnO thin films deposited by sol-gel spin-coating technique, Optik 158 (2018) 1342–1348.

[36] H. Rietveld, A profile refinement method for nuclear and magnetic structures, J. Appl. Crystallogr. 2 (1969) 65–71.

[37] M.J. McKelvy, R. Sharma, A.V.G. Chizmeshya, R.W. Carpenter, K. Streib, Magnesium hydroxide dehydroxylation: in situ nanoscale observations of lamellar nucleation and growth, Chem. Mater. 13 (2001) 921–926.

[38] F.V. Motta, A.P.A. Marques, M.S. Li, M.F.C. Abreu, C.A. Paskocimas, M.R.D. Bomio, R.P. Souza, J.A. Varela, E. Longo, Preparation and photoluminescence characteristics of In(OH)3: xTb3 + obtained by microwave-assisted hydrothermal method, J. Alloy. Compd. 553 (2013) 338–342.

[39] S.D. Birajdar, R.C. Alange, S.D. More, V.D. Murumkar, K.M. Jadhav, Sol-gel auto combustion synthesis, structural and magnetic properties of Mn doped ZnO nanoparticles, Procedia Manuf. 20 (2018) 174–180.

[40] S. Husain, L.A. Alkhtaby, E. Giorgetti, A. Zoppi, M. Muniz Miranda, Effect of Mn doping on structural and optical properties of sol gel derived ZnO nanoparticles, J. Lumin. 145 (2014) 132–137.

[41] S. Muthukumaran, R. Gopalakrishnan, Structural, FTIR and photoluminescence studies of Cu doped ZnO nanopowders by co-precipitation method, Opt. Mater. 34 (2012) 1946–1953.

[42] Y. Guo, X. Cao, X. Lan, C. Zhao, X. Xue, Y. Song, Solution-based doping of manganese into colloidal ZnO nanorods, J. Phys. Chem. C 112 (2008) 8832–8838.

[43] J. Huang, Q. Liao, F. Wang, X. Huang, H. Zhu, Synthesis of Fe-doped alumina transparent ceramics by co-precipitation and vacuum sintering, Ceram. Int. 44 (2018) 799–804.

[44] A. Eshaghi, H. Moradi, Optical and photocatalytic properties of the Fe-doped TiO2 nanoparticles loaded on the activated carbon, Adv. Powder Technol.

[45] K. Kalantari, M. Kalbasi, M. Sohrabi, S.J. Royaee, Synthesis and characterization of N-doped TiO2 nanoparticles and their application in photocatalytic oxidation of dibenzothiophene under visible light, Ceram. Int. 42 (2016) 14834–14842.

[46] D. Sánchez-Rodríguez, M.G. Méndez Medrano, H. Remita, V. Escobar-Barrios, Photocatalytic properties of BiOCl-TiO2 composites for phenol photodegradation, J. Environ. Chem. Eng. 6 (2018) 1601–1612.

[47] C. Gautam, A.K. Yadav, V.K. Mishra, K. Vikram, Synthesis, IR and Raman spectroscopic studies of (Ba,Sr)TiO3; borosilicate glasses with addition of La2O3, Open J. Inorg. Non-Met. Mater. 2 (4) (2012) 8.

[48] M. Feng, Y. Liu, Z. Zhao, H. Huang, Z. Peng, The preparation of Fe doped triclinic-hexagonal phase heterojunction WO3 film and its enhanced photocatalytic reduction of Cr (VI), Mater. Res. Bull. (2018).

[49] M. Sathya, K. Pushpanathan, Synthesis and optical properties of Pb doped ZnO nanoparticles, Appl. Surf. Sci. 449 (2018) 346–357.

[50] K. Veerathangam, M. Senthil Pandian, P. Ramasamy, Photovoltaic performance of Pb-doped CdS quantum dots for solar cell application, Mater. Lett. 220 (2018) 74–77.

[51] E. Mendoza-Mendoza, A.G. Nuñez-Briones, L.A. García-Cerda, R.D. Peralta-Rodríguez, A.J. Montes-Luna, One-step synthesis of ZnO and Ag/ZnO heterostructures and their photocatalytic activity, Ceram. Int. 44 (2018) 6176–6180.

[52] M.A. Hernández-Carrillo, M.F. Torres-Ricárdez, M.F. García-Mendoza, E. Ramírez-Morales, L. Rojas-Blanco, L.L. Díaz-Flores, G.E. Sepúlveda-Palacios, F. Paraguay-Delgado, G. Pérez-Hernández, Eu-modified ZnO nanoparticles for applications in photocatalysis, Catal. Today.

[53] M.A. Green, Intrinsic concentration, effective densities of states, and effective mass in silicon, J. Appl. Phys. 67 (1990) 2944–2954.

[54] A. Sarkar, S. Ghosh, S. Chaudhuri, A.K. Pal, Studies on electron transport properties and the Burstein-Moss shift in indium-doped ZnO films, Thin Solid Films 204 (1991) 255–264.

[55] S.N. Sarangi, G.K. Pradhan, D. Samal, Band gap engineering in SnO2 by Pb doping, J. Alloy. Compd. 762 (2018) 16–20.

[56] R. Yang, H. Sun, J. Li, Ya Li, Structural, magnetic and photocatalytic properties of Sr2 + doped BiFeO3 nanofibres fabricated by electrospinning, Ceram. Int. 44 (2018) 14032–14035.

[57] T.H. Le, A.T. Bui, T.K. Le, The effect of Fe doping on the suppression of photocatalytic activity of ZnO nanopowder for the application in sunscreens, Powder Technol. 268 (2014) 173–176.

[58] M. Mittal, A. Gupta, O.P. Pandey, Role of oxygen vacancies in Ag/Au doped CeO2 nanoparticles for fast photocatalysis, Sol. Energy 165 (2018) 206–216.

[59] M. Stefan, C. Leostean, O. Pana, D. Toloman, A. Popa, I. Perhaita, M. Senilă, O. Marincas, L. Barbu-Tudoran, Magnetic recoverable Fe3O4-TiO2:Eu composite nanoparticles with enhanced photocatalytic activity, Appl. Surf. Sci. 390 (2016) 248–259.

[60] J. Shi, G. Chen, G. Zeng, A. Chen, K. He, Z. Huang, L. Hu, J. Zeng, J. Wu, W. Liu, Hydrothermal synthesis of graphene wrapped Fe-doped TiO2 nanospheres with high photocatalysis performance, Ceram. Int. 44 (2018) 7473–7480.

[61] H. Liu, M. Li, J. Yang, C. Hu, J. Shang, H. Zhai, In situ construction of conjugated polymer P3HT coupled hierarchical ZnO composite with Z-scheme enhanced visible-light photocatalytic activity, Mater. Res. Bull. 106 (2018) 19–27.

[62] A. Fahami, G.W. Beall, Mechanosynthesis of carbonate doped chlorapatite–ZnO nanocomposite with negative zeta potential, Ceram. Int. 41 (2015) 12323–12330.

[63] Q. Ying, Y. Hao, Z. Wang, X. Li, Facile one-step preparation of triethanolamine modified magnetic nanoparticles for the high-efficient removal of Cu (II) ions and methylene blue, J. Taiwan Inst. Chem. Eng. (2018).

[64] M. Zare, K. Namratha, K. Byrappa, D.M. Surendra, S. Yallappa, B. Hungund, Surfactant assisted solvothermal synthesis of ZnO nanoparticles and study of their antimicrobial and antioxidant properties, J. Mater. Sci. Technol. 34 (2018) 1035–1043.

[65] T. Xia, M. Kovochich, M. Liong, L. Mädler, B. Gilbert, H. Shi, J.I. Yeh, J.I. Zink, A.E. Nel, Comparison of the mechanism of toxicity of zinc oxide and cerium oxide nanoparticles based on dissolution and oxidative stress properties, ACS Nano 2 (2008) 2121–2134.

[66] A.V. Badarinath, K. Mallikarjuna Rao, C. Madhu Sudhana Chetty, S. Ramkanth, T.V.S. Rajan, K. Gnanaprakash, A review on In-vitro antioxidant methods: comparisions, correlations and considerations, Int. J. PharmTech Res. 2 (2010) 1276–1285.

[67] S.M. Dizaj, F. Lotfipour, M. Barzegar-Jalali, M.H. Zarrintan, K. Adibkia, Antimicrobial activity of the metals and metal oxide nanoparticles, Mater. Sci. Eng.: C 44 (2014) 278–284.

[68] Y. Xie, Y. He, P.L. Irwin, T. Jin, X. Shi, Antibacterial activity and mechanism of action of zinc oxide nanoparticles against Campylobacter jejuni, Appl. Environ. Microbiol. 77 (2011) 2325–2331.

[69] M. Li, L. Zhu, D. Lin, Toxicity of ZnO nanoparticles to Escherichia coli: mechanism and the influence of medium components, Environ. Sci. Technol. 45 (2011) 1977–1983.

[70] N.M. Franklin, N.J. Rogers, S.C. Apte, G.E. Batley, G.E. Gadd, P.S. Casey, Comparative toxicity of nanoparticulate ZnO, bulk ZnO, and ZnCl2 to a freshwater microalga (Pseudokirchneriella subcapitata): the importance of particle solubility, Environ. Sci. Technol. 41 (2007) 8484–8490.

[71] J. Ma, A. Hui, J. Liu, Y. Bao, Controllable synthesis of highly efficient antimicrobial agent-Fe doped sea urchin-like ZnO nanoparticles, Mater. Lett. 158 (2015) 420–423.